Journal of Power Sources 204 (2012) 106–115

Contents lists available at SciVerse ScienceDirect

Journal of Power Sources

journal homepage: www.elsevier.com/locate/jpowsour

The influence of interconnect ribs on the performance of planar solid oxide fuel cell and formulae for optimal rib sizes

Wei Kong[a], Jiayu Li[b], Shixue Liu[c], Zijing Lin[a,b,*]

[a] Department of Physics and National Synchrotron Radiation Laboratory, University of Science and Technology of China, Hefei 230026, China
[b] Hefei National Laboratory for Physical Sciences at the Microscale, University of Science and Technology of China, Hefei 230026, China
[c] INAMORI Frontier Research Center, Kyushu University, Fukuoka 819-0395, Japan

ARTICLE INFO

Article history:
Received 31 October 2011
Received in revised form
26 December 2011
Accepted 1 January 2012
Available online 10 January 2012

Keywords:
Solid oxide fuel cell
Multiphysics numerical model
Interconnect rib
Contact resistance
Design optimization

ABSTRACT

A comprehensive mathematical model for the planar solid oxide fuel cell (SOFC) stack is presented. The model couples the intricate interdependency among the ionic conduction, electronic conduction, gas transport and the electrochemical reaction and takes into account the contact resistance between the electrode and interconnect rib and the dependence of the effective electrode properties on the microstructure parameters of the porous electrode. The validity of the mathematical model is demonstrated by the excellent agreement between the numerical and experimental *I–V* curves. Based on a standard set of model parameters, the cell performance is examined by systematically varying the rib width, contact resistance, fuel composition electrode properties and the pitch width. The results show conclusively that the cell output depends strongly on the rib width and a suitable choice of the rib width is important for realizing the potential of a SOFC stack. The optimal rib width is only sensitive to the contact resistance and the pitch width, but the optimal results for the anode and cathode ribs are quite different. Both the optimal anode and cathode rib widths depend linearly on the contact resistance and the pitch width and the parameters for the linearity are given.

© 2012 Elsevier B.V. All rights reserved.

1. Introduction

The anode-supported planar solid oxide fuel cell (pSOFC) is a promising new energy technology and has attracted increasing attention in the past years. It has long been reported that a single cell of pSOFC may produce a power density of 1 W cm^{-2} or higher at the operating temperature of 700–800 °C [1–6]. Although the performance of pSOFC at the single cell level is exciting, multiple cells must be connected in series by interconnect material to form a fuel cell stack for practical applications. Unfortunately, the performance of a pSOFC cell at a working stack level rarely exceeds a third of 1 W cm^{-2} [7]. The cell performance for small laboratory stacks can be higher, but significant reductions of power density due to the stack assembly are widely observed [8].

There are various factors that may affect the stack cell performance. One of the primary causes accounting for the lowered cell performance at the stack level is the additional losses caused by the interconnect geometry [8,9]. Small grooves in interconnect are commonly used as gas channels to carry the fuel and air flows. The ribs, which separate and define the channels, make direct contact with the electrodes. On the technical side, the channels and the ribs cannot be too small and the contact resistance between the ribs and the electrodes is part of the intrinsic property of the interconnect material [10]. In designing the layer architecture, there is a tradeoff that must be considered between the rib and channel sizes. On one hand, ribs covering bigger fraction of the cell area may reduce the interface resistance to current flow by increasing the electrode-interconnect contact area. Such ribs will give a better conduction of the electrical current and reduce ohmic losses. On the other hand, the chemical species do not diffuse as well underneath wide ribs. Narrow ribs and ribs covering small fraction of the cell area are needed to facilitate more uniform distribution of reactive gases across the area of the electrolyte surface and thus to promote electrochemical performance. The implication of the tradeoff to the cell performance can be very significant. It was reported that the power density was 0.76 W cm^{-2} at 0.7 V operating voltage for the combination of 2.6 mm channels and 2.4 mm ribs, when that for 4 mm channels and 1 mm ribs was as high as 1.03 W cm^{-2} [8]. Clearly, how to configure a channel network to improve the stack cell performance is highly consequential for the practical application [11] and is an important task of the pSOFC designer.

There have been a few theoretical studies investigating the impact of the rib size on the performance of solid oxide fuel cells. Ferguson et al. [12] gave a numerical example for the rib size effect

* Corresponding author at: Department of Physics, University of Science and Technology of China, Hefei 230026, China. Tel.: +86 551 3606345; fax: +86 551 3606348.
E-mail address: zjlin@ustc.edu.cn (Z. Lin).

0378-7753/$ – see front matter © 2012 Elsevier B.V. All rights reserved.
doi:10.1016/j.jpowsour.2012.01.041

on the performance of a specific electrolyte-supported SOFC. Tanner and Virkar proposed a simplified model to examine the effect of the interconnect design on the effective Ohmic resistance of the membrane-electrode assembly in an SOFC stack [13]. Lin et al. [14] described a phenomenological model and provided analytical expressions to estimate the rib effects on the concentration and ohimc polarizations of anode-supported SOFC stacks. Ji et al. [15] showed that the terminal output of a SOFC stack depended strongly on the contact resistance. Jeon et al. [16] described a microstructural model and examined the influence of the rib and pitch widths and the electrode-interconnect contact area specific resistance ($ASR_{contact}$) on the stack-cell performance. Based on systematic examination of the stack cell performance as a function of various influencing factors, Liu et al. [17] proposed a simple expression for the optimal rib width as a function of the pitch width and $ASR_{contact}$ that was independent of the porosity, layer thickness and conductivity of the electrode and easy to use for the SOFC engineers.

Unfortunately, the existing numerical studies on the effect of the rib size on the stack cell performance have been carried out with the assumption of equal width of the anode and cathode ribs and equal $ASR_{contact}$ for the anode-interconnect and cathode-interconnect interfaces. As a result, it is difficult to distinguish between the impacts of the anode rib and the cathode rib. As demonstrated experimentally by Kornely et al. [8], however, $ASR_{contact}$ for the anode-interconnect and cathode-interconnect interfaces can be very different and the impacts of the anode rib and the cathode rib on the stack cell performance are also very different. In fact, previous numerical studies have already shown very different effects of the cathode and anode ribs on the mass transport in the electrodes. For example, Liu et al. [17] reported that the anode gas transport of an anode-supported SOFC was only mildly affected by the anode rib, while an oxygen depletion zone of 0.46 mm was found with a cathode rib width of only 0.8 mm. The existing experimental and theoretical findings indicate clearly that the optimal design of the stack cell should use different widths for the anode and the cathode ribs.

Building upon the foundation of significant earlier literatures [18,19], this paper describes a two-dimensional microstructure based multi-physics model for SOFCs with composite electrodes. The model couples the intricate interdependency among the ionic conduction, electronic conduction, gas transport in porous electrodes and the electrochemical reaction processes in the functional layers and at the electrode/electrolyte interfaces. The impacts of the anode and cathode ribs are examined independently and for different electrode-interconnect contact resistances, fuel compositions, electrode porosities, electrode thicknesses and electrode conductivities. The optimal cathode and anode rib sizes for different $ASR_{contact}$ are obtained and parameterized to provide an easy-to-use guidance for designing the rib-channel layout.

2. Method

2.1. Physical model

A repeating cell unit of a pSOFC stack is shown schematically in Fig. 1a. The repeating unit consists of (i) cathode-side interconnect plate and the air channels, (ii) positive electrode (cathode)–electrolyte–negative electrode (anode) assembly, or PEN for short, (iii) anode-side interconnect plate and the fuel channels. A PEN assembly with composite electrodes often consists of five layers: (1) an anode support layer (ASL) that also acts as the anode current collector, (2) an anode functional layer (AFL) for reducing the activation losses by affording abundant three phase boundaries (TPBs), (3) an electrolyte layer, (4) a cathode functional layer (CFL), and (5) a cathode current collector layer

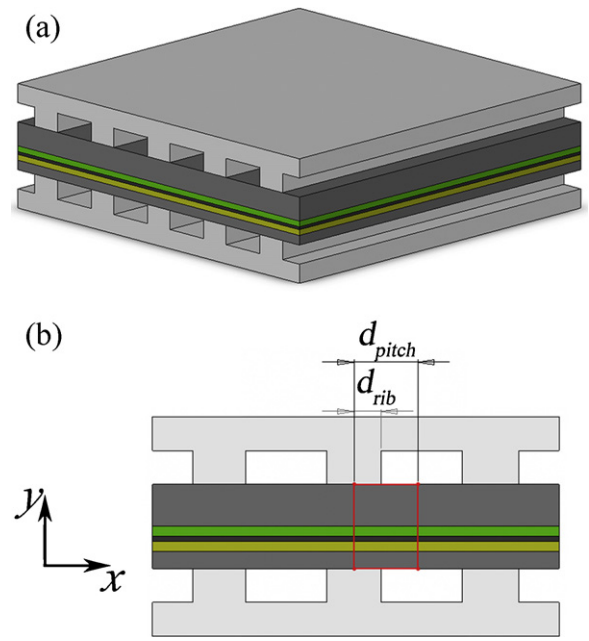

Fig. 1. Schematic of (a) an anode-supported planar SOFC stack cell unit, (b) a cross-section of the SOFC stack cell unit.

(CCCL). A cross section of the repeating stack cell unit is shown in Fig. 1b.

For simplicity, the stack cell is assumed to be in an isothermal steady state. As demonstrated before [17,19], a 2D model is equivalent to a 3D model when discussing the effects of rib sizes on the fuel cell performance as they provide essentially the same results. Therefore, a 2D model (Fig. 1b) is used here. Moreover, we assume the electrical conductivity of the interconnect is sufficiently high and the ohmic loss inside the interconnect (excluding the ohmic loss caused by the electrode-interconnect contact resistance) is negligible. Taking into account the equivalency of the repeating rib-channel pairs (pitches), the computational domain consists of only half of the repeating rib-channel pair, shown in Fig. 1b as inside the red square. The square computational domain has a width of d_{pitch} (the sum of one half of the rib width, d_{rib}, and one half of the channel width, $d_{channel}$) and a height of the total PEN thickness. The computational domain represents a repeating unit in a pSOFC cell of any size. Notice that we have implicitly assumed here that the anode and cathode pitch widths are equal, even though the widths for the anode rib (d_{rib}^{an}) and cathode rib (d_{rib}^{ca}) may be different. As the gas transports inside the anode and the cathode are practically independent from each other, the above implicit assumption for numerical convenience should not put any practical limitation on the modeling result. Indeed, previous 3D modeling studies [19] have shown that the rib effects on the overall stack cell output are basically the same whether the stack cell has a co-flow, counter-flow or cross-flow configuration.

The actual cell operating voltage (V_{op}) is lower than the ideal cell potential (Nernst potential) due to various polarizations such as activation polarization, ohmic polarization and concentration polarization. For the physical model described above, the V_{op} of the stack cell may be formally expressed as:

$$V_{op} = E_0 - \eta_{ASR}^{an} - \eta_{conc}^{an} - \eta_{act}^{an} - \eta_{ohm}^{an} - \eta_{ohm}^{el} - \eta_{ohm}^{ca} - \eta_{act}^{ca} - \eta_{conc}^{ca} - \eta_{ASR}^{ca} \quad (1)$$

where E_0 is the Nernst potential, η_{ASR}^{an} (η_{ASR}^{ca}) the anode-rib (cathode-rib) interface overpotential due to the contact resistance at the material boundary, η_{conc}^{an} (η_{conc}^{ca}) the anode (cathode) concentration polarization due to the resistance to the transport of fuel

(air) species through the porous electrode, η_{act}^{an} (η_{act}^{ca}) the anode (cathode) activation polarization due to the energy barrier for the electrochemical reactions, η_{ohm}^{an}, η_{ohm}^{el} and η_{ohm}^{ca} the ohmic polarizations in the anode, electrolyte and cathode associated with the ohmic resistances of the electrolyte and electrodes. The detailed model for each of the polarizations will be described later.

2.2. Governing equations for gas transport in porous electrodes

The mass transport of gas species in a porous medium is complex and includes three distinct mass-transfer mechanisms: Knudsen diffusion, molecular diffusion, as well as viscous flow. Thus, the dusty gas model is required to estimate accurately the gas transport in SOFC porous electrodes [20–22]. For a binary component system (fuel with H_2 and H_2O, or air with O_2 and N_2), the total molar flux of species i (i = 1, 2) may be written as [16,22,23],

$$N_i = -\frac{D_{12}^{eff} D_{iK}^{eff}}{D_{12}^{eff} + x_1 D_{2K}^{eff} + x_2 D_{1K}^{eff}} \nabla c_i - c_i \left(\frac{D_{1K}^{eff} D_{2K}^{eff}}{RTc_{tot}(D_{12}^{eff} + x_1 D_{2K}^{eff} + x_2 D_{1K}^{eff})} + \frac{k}{\mu} \right) \nabla p = -D_i \nabla c_i - c_i \frac{k' \nabla p}{\mu} = N_i^{diffusion} + N_i^{convection} \quad (2)$$

where c_i is the molar concentration of species i, c_{tot} ($= c_1 + c_2$) the total molar concentration of the binary mixture, $x_i (= c_i/c_{tot})$ the molar fraction of species i, R the universal gas constant, T the absolute temperature, p the total gas pressure, k the permeability coefficient, μ the viscosity coefficient, D_{iK}^{eff} the effective Knudsen diffusion coefficient of species i and D_{ij}^{eff} the effective binary diffusion coefficient. $D_i (= (D_{12}^{eff} D_{iK}^{eff})/(D_{12}^{eff} + x_1 D_{2K}^{eff} + x_2 D_{1K}^{eff}))$ is the equivalent diffusion coefficient of species i and $k' (= k + (\mu D_{1K}^{eff} D_{2K}^{eff})/(RTc_{tot}(D_{12}^{eff} + x_1 D_{2K}^{eff} + x_2 D_{1K}^{eff})))$ is the equivalent permeability coefficient of the binary system. D_{ij}^{eff} and D_{iK}^{eff} may be evaluated by the following equations.

$$D_{ij}^{eff} = \frac{\varepsilon}{\tau} \frac{3.198 \times 10^{-8} T^{1.75}}{p\left(\nu_i^{1/3} + \nu_j^{1/3}\right)^2} \left(\frac{1}{M_i} + \frac{1}{M_j} \right)^{0.5} \quad (3)$$

$$D_{iK}^{eff} = \frac{\varepsilon}{\tau} \frac{2}{3} r_g \sqrt{\frac{8RT}{\pi M_i}} \quad (4)$$

$$r_g = \frac{2}{3} \frac{\varepsilon}{1-\varepsilon} \frac{1}{\phi_{el}/r_{el} + \phi_{io}/r_{io}} \quad (5)$$

where ε is the porosity, τ the tortuosity factor, r_g the pore radius, ν_i and M_i the diffusion volume and molar mass of species i, respectively. r_{el} (r_{io}) is the mean electronic (ionic) conducting particle's radii, ϕ_{el} (ϕ_{io}) the volume fraction of the electronic (ionic) conducting particles in the composite electrode material.

The molar mass conservation equation of species i is given by:

$$\nabla \cdot N_i = \begin{cases} 0 & \text{in } ASL \text{ or } CCCL \\ R_i & \text{in } AFL \text{ or } CFL \end{cases} \quad (6)$$

where R_i is the molar rate of production or consumption of species i due to the electrochemical reaction.

2.3. Governing equations for electrical processes

Electronic and ionic current densities are governed by the charge continuity equations associated with the Ohm's law

$$\nabla \cdot i_{el} = \nabla \cdot (-\sigma_{el}^{eff} \nabla \varphi_{el}) = \begin{cases} 0 & \text{in } ASL \text{ or } CCCL \\ -S_{current} & \text{in } AFL \\ S_{current} & \text{in } CFL \end{cases} \quad (7)$$

$$\nabla \cdot i_{io} = \nabla \cdot (-\sigma_{io}^{eff} \nabla \varphi_{io}) = \begin{cases} S_{current} & \text{in AFL} \\ 0 & \text{in electrolyte} \\ -S_{current} & \text{in CFL} \end{cases} \quad (8)$$

where i_{el} (i_{io}) is the electronic (ionic) current density vector, φ_{el} (φ_{io}) the electronic (ionic) potential, $S_{current}$ the current source. For the charge conservation, the source of electronic current is also the sink of ionic current. σ_{el}^{eff} (σ_{io}^{eff}) is the effective electronic (ionic) conductivity of the porous electrode layer. The effective electronic and ionic conductivities of composite electrode are dependent on structural parameters such as particle size, porosity, component volume fractions. The relationship between the effective electrode properties and the microstructure parameters may be obtained by the coordination number theory based percolation model [24–27]. For a binary system with random packing of spheres, the effective electric conductivity of k-phase is estimated as [28],

$$\sigma_k^{eff} = \sigma_k^0 \left(\frac{\phi_k - \phi_k^t}{1 + \varepsilon/(1-\varepsilon) - \phi_k^t} \right)^2 \quad (9)$$

where σ_k^0 is the electric conductivity of k-material in dense solid. ϕ_k is the volume fraction of the k-particles in the solid structure, ϕ_k^t the percolation threshold volume fraction of the k-particles which is determined by [26,29],

$$Z \frac{\phi_{el}^t / r_{el}}{\phi_{el}^t / r_{el} + (1 - \phi_{el}^t)/r_{io}} = 1.764 \quad (10)$$

$$Z \frac{\phi_{io}^t / r_{io}}{(1 - \phi_{io}^t)/r_{el} + \phi_{io}^t / r_{io}} = 1.764 \quad (11)$$

where Z is the average coordination number for each particle and set as 6 for a random packing of spheres [29–31]. σ_k^0 (Ω^{-1} m^{-1}) for Ni, LSM and YSZ are estimated respectively as [16,32],

$$\sigma_{Ni}^0 = 3.27 \times 10^6 - 1065.3T \quad (12)$$

$$\sigma_{LSM}^0 = \frac{4.2 \times 10^7}{T} \exp\left(\frac{-1150}{T}\right) \quad (13)$$

$$\sigma_{YSZ}^0 = 6.25 \times 10^4 \exp\left(\frac{-10300}{T}\right) \quad (14)$$

The remaining quantity in Eqs. (7) and (8), $S_{current}$, may be calculated as,

$$S_{current} = \lambda_{TPB} i_{trans} \quad (15)$$

where λ_{TPB} is the TPB length per unit volume (mm^{-3}) or unit area (mm^{-2}) of AFL or CFL, and i_{trans} is the charge transfer current per TPB length. The volume-specific TPB length λ_{TPB} can be written as [16],

$$\lambda_{TPB}^V = 2\pi \min(r_{el}, r_{io}) \sin\left(\frac{\theta}{2}\right) n_{el}^V Z_{el-io} P_{el} P_{io} \quad (16)$$

where $n_{el}^V = ((1-\varepsilon)\phi_{el})/(4\pi r_{el}^3/3)$ is the number of electronic conducting particles per unit volume of the electrode function layer, θ is the contact angle between particles (θ is assigned as 30°) [29], P_k ($k = el, io$) is the percolation probability of k-particle, Z_{j-k} ($j, k = el,$

io) is the average number of contacts between a j-particle and k-particle. P_k and Z_{j-k} are calculated as,

$$P_k = \left(1 - \left(\frac{3.764 - Z_{k,k}}{2}\right)^{2.5}\right)^{0.4} \tag{17}$$

$$Z_{k,k} = Z\frac{\phi_k/r_k}{\phi_{el}/r_{el} + \phi_{io}/r_{io}} \tag{18}$$

$$Z_{j-k} = \frac{Z}{2}\left(1 + \frac{r_j^2}{r_k^2}\right)\frac{\phi_k/r_k}{\phi_{el}/r_{el} + \phi_{io}/r_{io}} \tag{19}$$

The area-specific TPB length, λ_{TPB}^A, may be written as [16]

$$\lambda_{TPB}^A = 4\pi r_{el}\sin\left(\frac{\theta}{2}\right) r_{el} n_{el}^V P_{el} \tag{20}$$

The charge transfer current density, i_{trans}, may be calculated according to the empirical Butler–Volmer equation. For Ni/YSZ AFL TPBs, i_{trans} is calculated as [33,34],

$$i_{trans}^{an} = i_{ref}^{an}\exp\left(-\frac{E_{H_2}}{R}\left(\frac{1}{T} - \frac{1}{T_{ref}}\right)\right)\left(\frac{p_{H_2}^{TPB}p_{H_2O}^{TPB}}{p_{H_2}^0 p_{H_2O}^0}\right) \times \left[\exp\left(\frac{2\alpha_f^{an}F}{RT}\eta_{act}^{an}\right) - \exp\left(-\frac{2\beta_r^{an}F}{RT}\eta_{act}^{an}\right)\right] \tag{21}$$

For LSM/YSZ CFL TPBs, i_{trans} is calculated as [33,34]

$$i_{trans}^{ca} = i_{ref}^{ca}\exp\left(-\frac{E_{O_2}}{R}\left(\frac{1}{T} - \frac{1}{T_{ref}}\right)\right)\left(\frac{p_{O_2}^{TPB}}{p_{O_2}^0}\right)^{0.25} \times \left[\exp\left(\frac{2\alpha_f^{ca}F}{RT}\eta_{act}^{ca}\right) - \exp\left(-\frac{2\beta_r^{ca}F}{RT}\eta_{act}^{ca}\right)\right] \tag{22}$$

Here α_f^{an} (α_f^{ca}) and β_r^{an} (β_r^{ca}) are the anode (cathode) forward and reverse reaction symmetric factors, respectively. E_{H_2} (E_{O_2}) is the activation energy for the anode (cathode) electrochemical reaction. Parameters i_{ref}^{an} and i_{ref}^{ca} are obtained from fitting experiments I–V relations. η_{act}^{an} and η_{act}^{ca} are respectively the anode and cathode activation polarizations and calculated as,

$$\eta_{act}^{an} = \varphi_{el} - \varphi_{io} - \eta_{conc}^{an} = \varphi_{el} - \varphi_{io} - \frac{RT}{2F}\ln\left(\frac{p_{H_2}^0}{p_{H_2O}^0}\frac{p_{H_2O}^{TPB}}{p_{H_2}^{TPB}}\right) \tag{23}$$

$$\eta_{act}^{ca} = \varphi_{io} - \varphi_{el} - \eta_{conc}^{ca} = \varphi_{io} - \varphi_{el} - \frac{RT}{4F}\ln\left(\frac{p_{O_2}^0}{p_{O_2}^{TPB}}\right) \tag{24}$$

where F is the Faraday constant, φ_{conc}^{an} (φ_{conc}^{ca}) the anode (cathode) concentration polarization, $p_{H_2}^0$ ($p_{H_2O}^0$) the partial pressure of H_2 (H_2O) at the fuel channel/anode interface, $p_{O_2}^0$ the partial pressure of O_2 at the air channel/cathode interface, $p_{H_2}^{TPB}$ ($p_{H_2O}^{TPB}$) the partial pressure of H_2 (H_2O) at the anode TPBs, and $p_{O_2}^{TPB}$ the partial pressure of O_2 at the cathode TPBs.

2.4. Boundary conditions (BCs)

As described above, gas transport equation, ionic conduction equation, electronic conduction equation and the Butler–Volmer equation are taken into account in this model. Proper settings of the boundary conditions are required to solve these coupled partial differential equations correctly. The boundary settings for the mass transport equations are shown in Table 1. The boundary settings for the electronic and ionic charge transfer equations are shown in Table 2. The contact resistance is set on the interface between the interconnect ribs and the electrodes. That is, local current densities cross the rib/anode ($i_{rib\to ASL}$) and the cathode/rib ($i_{CCCL\to rib}$) interfaces are determined by

$$i_{rib\to ASL} = \frac{\varphi_{e,rib/ASL} - \varphi_{e,ASL/rib}}{ASR_{contact}^{an}} \tag{25}$$

$$i_{CCCL\to rib} = \frac{\varphi_{e,CCCL/rib} - \varphi_{e,rib/CCCL}}{ASR_{contact}^{ca}} \tag{26}$$

where $ASR_{contact}^{an}$ ($ASR_{contact}^{ca}$) is the area specific contact resistance at the rib-anode (cathode) interface, $\varphi_{e,rib/ASL}$ ($\varphi_{e,ASL/rib}$) is the electric potential at the rib (anode) side of the anode-rib boundary, $\varphi_{e,CCCL/rib}$ ($\varphi_{e,rib/CCCL}$) is the electric potential at the cathode (rib) side of the cathode-rib boundary. It should be pointed out that the contact resistance is an effective model parameter that may come from various origins such as the oxide scale formation of the interconnect material and the loose contact between the cell components.

2.5. Numerical solution

The model was implemented in the finite element commercial software COMSOL MULTIPHYSICS® Version 3.5. Structured mesh elements were used and consisted of 1152 rectangles with 42,487 degrees of freedom. The direct solver (UMFPACK) was used to solve the coupled partial differential equations of electronic, ionic and gas transport with a relative convergence tolerance of 1×10^{-6}. Subtle features in the numerical solution process worthy mentioning also include: (1) As the electrochemical reaction in the region of CFL underneath the rib may lead to negative partial pressure of oxygen and cause numerical failure, oxygen molar fraction was set as $x_{O_2} = \max(x_{O_2}, 10^{-9})$ to avoid the numerical instability; (2) Similarly, the activation polarizations, η_{act}^{an} and η_{act}^{ca}, were set to be non-negative values, $\eta_{act}^{an} = \max(\eta_{act}^{an}, 0)$ and $\eta_{act}^{ca} = \max(\eta_{act}^{ca}, 0)$, to comply with the physical requirement.

2.6. Model parameters and numerical validation

The platinum or silver meshes are the typical interconnect for single cell testing. The meshes may be regarded as interconnect ribs with small pitch widths. A pitch width of 0.2 mm and a rib width of 0.05 mm corresponding to the experimental description were used here for the numerical model validation. The material property parameters as deduced before [23] and the experimental operating conditions of Zhao and Virkar [2] are listed in Table 3. Notice that, as the fuel and air utilization rates are often negligible in the single cell testing, the same molar concentrations of gas species are used in the BCs of the mass transports for obtaining the I–V relations. Based on the parameters in Table 3 and assuming the total contact resistance (the sum of $ASR_{contact}^{an}$ and $ASR_{contact}^{ca}$) of the cell are respectively 0.0132 Ω cm^2, 0.0272 Ω cm^2 and 0.1 Ω cm^2 for 800 °C, 700 °C and 600 °C, the simulated I–V relations are compared with the experimental results of Zhao and Virkar in Fig. 2. As shown in Fig. 2, the theoretical results agree with the experimental measurements very well. It is worthy mentioning that Zhao and Virkar have estimated the total contact resistance to be 0.053 Ω cm^2 at 800 °C, which is quite different from that used in our model. Nevertheless, the parameter used in the numerical model and the experimental estimate are in fact consistent with each other. The contact resistance estimated by Zhao and Virkar only corresponds to an equivalent contact resistance for the interconnect current collection as they attributed the contact resistance to be distributed over the entire pitch width instead of only the rib width. As the current only flow through the electrode/rib interface, the equivalent contact resistance for our numerical model would correspond to $ASR_{contact}^{equ} \approx (ASR_{contact}^{an} + ASR_{contact}^{ca})d_{pitch}/d_{rib} =$

Table 1
Boundary condition (BC) settings for mass transports in electrodes ("Insulation" means no flux through the boundary).

Equations	Boundary	ASL/channel interface		AFL/electrolyte interface		All others
	BC type	H_2 molar concentration	H_2O molar concentration	H_2 Inward molar flux	H_2O Inward molar flux	
Fuel transfer	BC	$c^0 = p^0_{H_2}/R/T$	$c^0 = p^0_{H_2O}/R/T$	$-i^{an}_{trans}\lambda^A_{TPB}/2F$	$i^{an}_{trans}\lambda^A_{TPB}/2F$	Insulation
Equation	Boundary	CCCL/channel interface		CFL/electrolyte interface		All others
	BC type	O_2 molar concentration	N_2 molar concentration	O_2 Inward molar flux	N_2 Inward molar flux	
Air transfer	BC	$c^0 = p^0_{O_2}/R/T$	$c^0 = p^0_{N_2}/R/T$	$-i^{ca}_{trans}\lambda^A_{TPB}/4F$	0	Insulation

Table 2
Boundary settings for the electronic and ionic charge transfer equations ("Electric Insulation" means that the normal component of the electric current is zero).

Equations	Boundary BC type	Rib/CCCL interface Reference potential ($\varphi_{e,rib/CCCL}$)	Rib/ASL interface Reference potential ($\varphi_{e,rib/ASL}$)	CFL/electrolyte interface Inward current flow	AFL/electrolyte interface Inward current flow	All others
Electronic transfer	BC	V_{op}	E_0 (=1.122V)	$i^{ca}_{trans}\lambda^A_{TPB}$	$-i^{an}_{trans}\lambda^A_{TPB}$	Electric insulation
Equations	Boundary BC Type	Rib/CCCL interface	Rib/ASL interface	CFL/electrolyte interface Interior current source	AFL/electrolyte interface Interior current source	All others
Ionic transfer	BC			$-i^{ca}_{trans}\lambda^A_{TPB}$	$i^{an}_{trans}\lambda^A_{TPB}$	Electric insulation

$0.0132\ \Omega\ \text{cm}^2 * 0.2/0.05 \approx 0.053\ \Omega\ \text{cm}^2$, in agreement with the experimental estimation.

The good agreement between the theoretical and experimental results demonstrates that the theoretical model is capable of reliably predicting the fuel cell performance in practical operations. Hence, the numerical model is used in the following to examine the influence of interconnect rib on the performance of planar SOFC. Moreover, except for those specified explicitly for each testing case, the model parameters listed in Table 3 are used throughout the paper.

3. Results and discussion

3.1. Performances of cells with ribs

The influence of the interconnect configurations on the cell performance was first examined with two cells having different pitch widths but the same rib to pitch width ratios. One cell (single cell) has a pitch width (d_{pitch}), an anode rib width (d^{an}_{rib}) and a cathode rib width (d^{ca}_{rib}) of 0.2, 0.05 and 0.05 mm, respectively. The corresponding parameters for the other cell (stack cell) are 2, 0.5 and 0.5 mm, respectively. Even though all the other model parameters and boundary settings are the same, as shown in Tables 1–3, the output current density of the stack cell is only 6011 A m^{-2}, a reduction of 19% from the single cell output of 7381 A m^{-2}. Clearly, the cell performance is strongly influenced by the pitch width and a small pitch width is beneficial for increasing the cell output. The observation is consistent with the analytical and numerical analyses reported before [14,17].

The substantial difference between the performances of the single cell and the stack cell may be understood by the difference in their fuel and oxidant species' distributions. As shown in Fig. 3a, the distributions of H_2 and O_2 in the single cell is reasonably uniform at the electrode-electrolyte interfaces as its rib width (50 μm)

Table 3
Basic model parameters for the reference cell [23].

Operating parameter	T	V_{op}	$p^0_{H_2}$	$p^0_{O_2}$	$p^0_{O_2}$
	700 °C	0.7 V	0.97 atm	0.03 atm	0.21 atm
Cell component	CCCL	CFL	Electrolyte	AFL	ASL
Thickness (μm)	50 [2]	20 [2]	8 [2]	20 [2]	1000 [2]
ε	45% [2]	26% [2]		23% [2]	48% [2]
ϕ_{el}	100% [2]	47.5% [2]		55% [2]	55% [2]
σ^{eff}_{el} (Sm^{-1})	$4{,}05 \times 10^3$ (800 °C) 4.00×10^3 (700 °C) 3.90×10^3 (600 °C)	25.5 (800 °C) [2] 25.0 (700 °C) 24.4 (600 °C)		1413 (800 °C) 1484 (700 °C) 1555 (600 °C)	430 (800 °C) [2] 451 (700 °C) 473 (600 °C)
σ^{eff}_{io} (Sm^{-1})		0.36 (800 °C) 0.14 (700 °C) 0.04 (600 °C)	4.2 (800 °C) [2] 1.6 (700 °C) [2] 0.47 (600 °C)	0.31 (800 °C) 0.12 (700 °C) 0.04 (600 °C)	
r_{el}/r_{io}	1	1.85		2.71	2.71
r_{io} (μm)	0.6	0.2		0.2	0.3
E_{O_2} (J mol^{-1})		130×10^3 [34]			
$\alpha^{ca}_f, \beta^{ca}_r$		0.65, 0.35			
$i^{ca}_{0,ref}$ (A m^{-1})		1.25×10^{-4}			
E_{H_2} (J mol^{-1})				120×10^3 [33,34]	
$\alpha^{an}_f, \beta^{an}_r$				1, 0.5 [33,34]	
$i^{an}_{0,ref}$ (A m^{-1})				8.0×10^{-3}	
τ	3	3		3	3
$ASR^{an}_{contact}$ (Ω cm^2)					0.01
$ASR^{ca}_{contact}$ (Ω cm^2)	0.01				

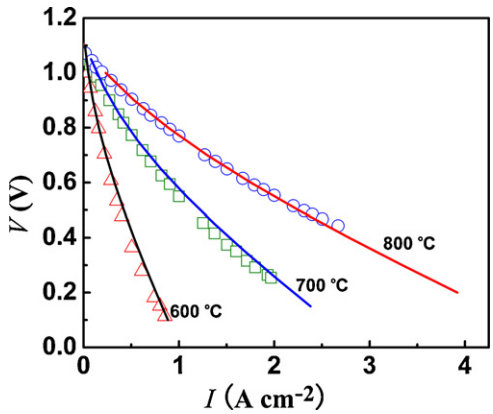

Fig. 2. Comparison of the theoretical and experimental *I–V* relationships at different operating temperatures. The open symbols and solid lines denote respectively the measured and the calculated results.

is comparable to the cathode layer thickness and very small compared to the anode layer thickness. Fig. 3b, however, shows a quite different situation for the stack cell as its rib width (500 μm) is over 7 times the cathode layer thickness. The O_2 concentration at the cathode TPB of the stack cell decreases from 2.5 mol m^{-3} under the channel to 0.56 mol m^{-3} under the middle of the rib. This is an important factor contributing to the reduced performance of the stack cell with a large pitch width. In the other hand, the H_2 concentration at the anode TPB of the stack cell is roughly constant at around 10.7 mol m^{-3} as the rib width is only about one half of the anode layer thickness. Clearly, the influences of the anode and cathode ribs on the gas transport are characteristically different. In

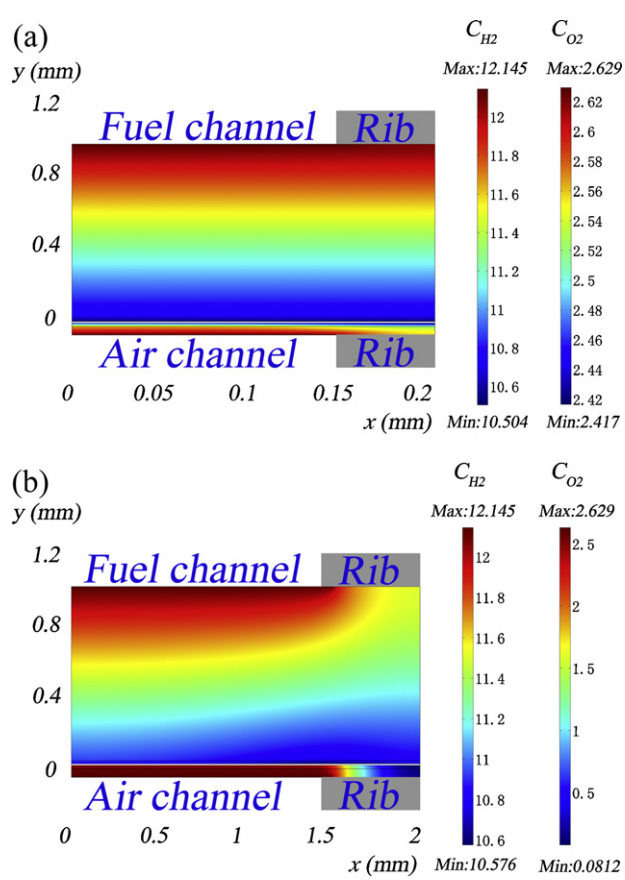

Fig. 3. Distributions of hydrogen and oxygen concentrations (mol m^{-3}) in (a) single cell, (b) stack cell.

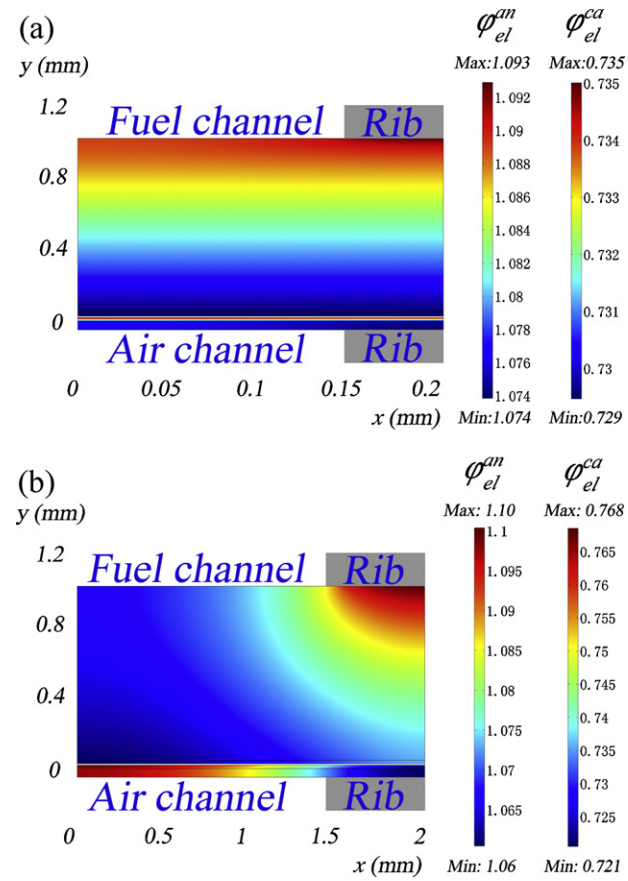

Fig. 4. The distributions of electric potentials in (a) single cell, (b) stack cell.

an anode-supported SOFC, the rib to pitch width ratio for the cathode should be relatively small in order to reduce the concentration polarization.

Another factor contributing to the reduced performance of the stack cell is the increased ohmic loss due to the elongated current conduction path associated with the large pitch width. Fig. 4 compares the distributions of electric potentials in the single cell and the stack cell. The potential variations inside the cathode and the anode of the single cell are 6 mV and 19 mV, respectively. The corresponding quantities for the stack cell are respectively 47 mV and 40 mV. The ohmic polarization of the stack cell anode is comparable to that of the cathode and is relatively large. As the effect of rib width on the anode concentration polarization is rather limited, there is more room for us to reduce the ohmic loss by increasing the anode rib width. Consequently, the desirable rib to pitch width ratio for the anode should be relatively large in comparison with that for the cathode. Evidently, the optimal rib to pitch width ratios for the anode and the cathode should not be constrained to a single value and should be searched separately.

3.2. The effect of anode rib size on the cell performance

To gain more insight into the effect of the anode rib size on the cell performance, the stack cell output for a fixed pitch width of 2 mm is examined by varying the rib width together with a few likely influential model parameters. The numerical results are shown in Fig. 5

The cell performance is affected by both the ohmic and concentration polarizations. It is natural to expect that the contact resistance at the rib–ASL interface is an influential parameter. Many efforts are devoted to reduce $ASR_{contact}$ to the desired level

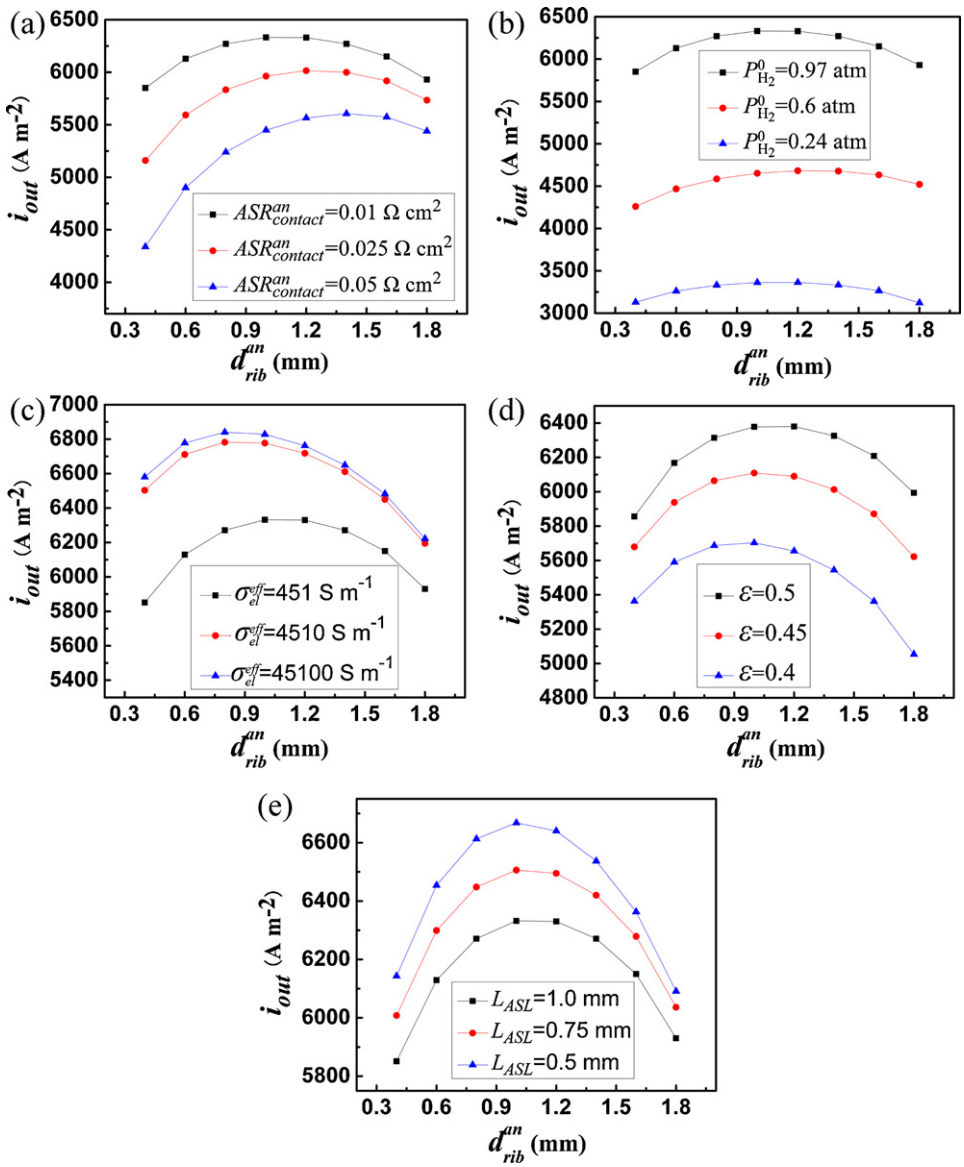

Fig. 5. The effect of anode rib size on the cell output current density (i_{out}) influenced by: (a) the contact resistance, (b) the fuel composition, (c) the electronic conductivity of ASL, (d) the porosity of ASL, and (e) the thickness of ASL.

of 0.01–0.05 Ω cm^2 [35]. Consequently, three representative values in this range, 0.01, 0.025 and 0.05 Ω cm^2, are used here. As may be seen in Fig. 5a, the maximal current densities for $ASR^{an}_{contact}$ of 0.01, 0.025 and 0.05 Ω cm^2 are 6339, 6018 and 5609 A m^{-2}, respectively, corresponding to the optimal rib widths of 1.1, 1.26 and 1.43 mm. As expected, the maximal cell output increases with the decrease of the contact resistance, while the optimal rib width increases with the increase of the contact resistance. Without the rib size optimization, e.g., for a fixed rib width of 0.4 mm, the output current densities for $ASR^{an}_{contact}$ of 0.01, 0.025 and 0.05 Ω cm^2 are respectively 7.7%, 14.3% and 22.7% less than their optimal values. Clearly, the anode rib width has a significant impact on the cell performance. The larger the contact resistance is, the more important the rib size optimization is. Moreover, the benefit gained through rib size optimization may substantially offset the shortcoming associated with the high $ASR_{contact}$. For example, the optimized output of 5609 A m^{-2} for $ASR^{an}_{contact}$ of 0.05 Ω cm^2 is 8.7% higher than that of 5160 A m^{-2} for $ASR^{an}_{contact}$ of 0.025 Ω cm^2 with a rib width of 0.4 mm. This result indicates that the advantage associated with the small contact resistance may be greatly reduced, or even lost completely, if the rib width is not chosen appropriately.

High fuel utilization is required in practical applications and the H_2 partial pressure changes substantially along the fuel channel. The rib size effect on the cell performance is examined here for three representative H_2 partial pressures, $p^0_{H_2}$ = 0.97, 0.6 and 0.24 atm. As shown in Fig. 5b, the cell outputs with a fixed rib width of 0.4 mm are 7.7%, 9.1% and 7.0% less than their optimal values for $p^0_{H_2}$ of 0.97, 0.6 and 0.24 atm, respectively. The results show that the impact of the rib size is not negligible for a wide range of $p^0_{H_2}$. Nevertheless, the influence of $p^0_{H_2}$ on the optimal rib width is moderate. The optimal rib widths are respectively 1.10, 1.28 and 1.12 mm for $p^0_{H_2}$ of 0.97, 0.6 and 0.24 atm. The current output with d^{an}_{rib} of 1.1 mm for $p^0_{H_2}$ = 0.6 atm is only 0.3% less than the optimal result. This is fortunate as the optimized anode rib design is of general applicability for different fuel operations.

The effective electronic conductivity (σ^{eff}_{el}) of ASL depends strongly on its material composition and microstructure such as the average conducting particle size and volume fraction and the porosity. For example, the measured electronic conductivity of ASL at 800 °C may vary from 430 S m^{-1} [2] to 60774 S m^{-1} [36] for seeming similar materials. Therefore, three representative values of σ^{eff}_{el},

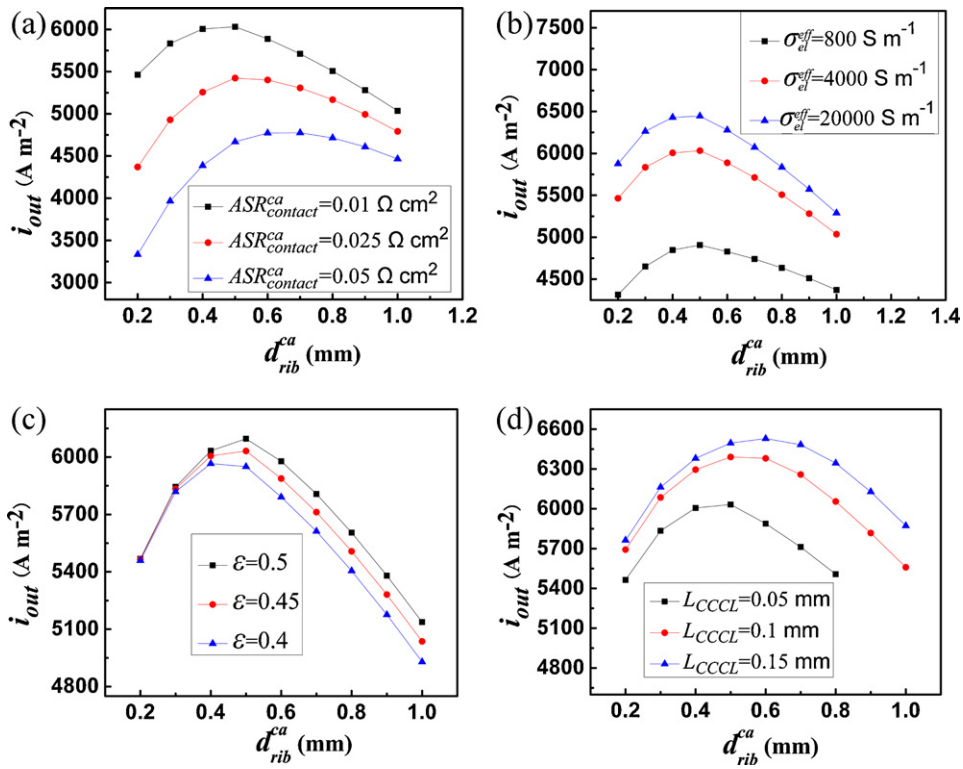

Fig. 6. The effect of cathode rib size on the cell output current density influenced by: (a) the contact resistance, (b) the electronic conductivity of CCCL, (c) the porosity of CCCL and (d) the thickness of CCCL.

451, 4510, 45100 S m^{-1}, are used here to examine their influence on the rib size effect on the cell performance. As shown in Fig. 5c, the output current densities for a fixed rib width of 0.4 mm are 5851, 6503 and 6580 A m^{-2} for σ^{eff}_{el} of 451, 4510, 45,100 S m^{-1}, respectively. With the rib width optimization, the output may increase to 6339, 6789 and 6846 A m^{-2}, or the increases of 8.3%, 4.4% and 4.0%, respectively. Hence, the rib size optimization is helpful for improving the cell performance for any practical σ^{eff}_{el}, but the improvement is more noticeable for low σ^{eff}_{el} of ASL. Moreover, although the optimal rib widths for σ^{eff}_{el} of 451, 4510, 45,100 S m^{-1} are respectively 1.1, 0.87 and 0.85 mm, the rib width of 1.1 mm is sufficiently optimal for any $\sigma^{eff}_{el} = 451$ S m^{-1} as the output is within 1% of the optimal value. Therefore, the rib width optimized for low σ^{eff}_{el} may be directly usable for the larger σ^{eff}_{el} cases. Another point worthy mentioning is the maximal cell output may increase by 7% when σ^{eff}_{el} is increased from 451 to 4510 S m^{-1}, but the output increase is less than 1% when σ^{eff}_{el} is increased from 4510 to 45100 S m^{-1}. Consequently, the effort to increase σ^{eff}_{el} beyond 4510 S m^{-1} is not very meaningful.

Fig. 5d shows the output current density as a function of the anode rib width for ASL with three different porosities. The cell outputs are seen to vary notably with the rib width for all the three porosities examined. The optimal rib width increases with the increase of the porosity for reduced gas transport resistance. However, the change of the optimal rib width with the porosity is rather modest and the optimal rib widths are 1.12, 1.08 and 1.04 mm for the porosity of 0.5, 0.45 and 0.4, respectively. If the rib width optimized for one of the three porosities is used for an ASL with the other porosity, the current output is different from its optimal value by less than 0.5%. Therefore, the optimal rib width may be viewed as independent of the ASL porosity in practice.

Fig. 5e shows the relationship between the output current density and the anode rib width for three ASL thicknesses. The rib size effect on the cell output is significant for all the three ASL thicknesses. The ASL thickness also has a significant effect on the cell output. However, the optimal rib widths for the three thicknesses are roughly the same, agreeing with the previous observation that the optimal rib width is independent of the ASL thickness as long as the thickness is larger than a few hundred microns [19].

3.3. The effect of cathode rib size on the cell performance

Fig. 6a shows the results on the variation of the output current density with the cathode rib width for different contact resistances. The maximal current densities for $ASR^{ca}_{contact}$ of 0.01, 0.025 and 0.05 Ω cm^2 are 6035, 5425 and 4785 A m^{-2}, respectively, corresponding to the optimal rib widths of 0.46, 0.56 and 0.67 mm. As discussed above, the optimal rib width for the anode is in the vicinity of 1 mm. Compared to the results obtained with a fixed cathode rib width of 1 mm, the rib width optimization increases the output current by 20%, 13% and 7.1% for $ASR^{ca}_{contact}$ of 0.01, 0.025 and 0.05 Ω cm^2, respectively. Clearly, the cathode rib width has a significant impact on the cell performance. Moreover, the optimal rib widths for the cathode and the anode are quite different.

Fig. 6b shows the results of the output current densities for three representative electronic conductivities of CCCL, σ^{eff}_{el} = 800, 4000, 20,000 S m^{-1}. The output current densities for a fixed cathode rib width of 1 mm are 4370, 5036 and 5289 A m^{-2} for σ^{eff}_{el} of 800, 4000, 20,000 S m^{-1}, respectively. With the rib width optimization, the outputs may increase to 4895, 6035 and 6453 A m^{-2}, or the increases of 12%, 20% and 22%, respectively. Evidently, the cathode rib size optimization is very helpful for improving the cell performance for any practical σ^{eff}_{el}, and the benefit often increases with the increased σ^{eff}_{el} of CCCL. As shown in Fig. 6b, however, although the

optimal cell output increases with the increased σ_{el}^{eff} of CCCL, the optimal cathode rib widths for σ_{el}^{eff} of 800, 4000, 20,000 S m^{-1} only vary slightly and are respectively 0.49, 0.46 and 0.45 mm. In fact, the rib width of 0.46 mm is sufficiently optimal for all σ_{el}^{eff} examined as the output is within 0.1% of the optimal value. Therefore, the rib width optimized for a medium σ_{el}^{eff} of CCCL (~4000 S m^{-1}) is representative for all practical σ_{el}^{eff} cases.

Fig. 6c shows the output current density as a function of the cathode rib width for CCCL with three different porosities. Similar to the case for the optimal anode rib sizes, the change of the optimal cathode rib width with the porosity is rather modest and the optimal cathode rib widths are 0.44, 0.46 and 0.48 mm for the porosity of 0.4, 0.45 and 0.5, respectively. If the rib width optimized for a porosity of 0.4 is used for a CCCL with a porosity of 0.5, the current output is different from its optimal value by less than 1%. Therefore, the optimal cathode rib width may be viewed as independent of the CCCL porosity.

Fig. 6d shows the relationship between the output current densities and the cathode rib width for three different CCCL thicknesses. As shown in the figure, the rib size effect on the cell output is significant for all the three CCCL thicknesses. The CCCL thickness also has a significant effect on the cell output. The maximal cell outputs are 6035, 6399 and 6528 A m^{-2} for the CCCL thicknesses of 0.05, 0.10 and 0.15 mm and are 20%, 15% and 11% higher than the outputs with a fixed cathode rib width of 1 mm, respectively. Some dependence of the optimal cathode rib width on the CCCL thickness is observed. The optimal rib widths are 0.46, 0.55 and 0.6 mm for the CCCL thickness of 50, 100 and 150 μm, respectively. However, the dependence of the optimal cathode rib width on the CCCL thickness is rather mild. If the rib width optimized for a CCCL thickness of 50 μm is used for a CCCL thickness of 150 μm, the current output is different from its optimal value by less than 1%. Therefore, the cathode rib width optimized for the CCCL thickness of 50 μm is sufficiently optimal for other practical CCCL thickness.

3.4. Expressions for the optimal rib widths

As discussed above, the output current density depends strongly on the rib width and a suitable choice of the rib width is very important for the high performance of a SOFC stack cell. The numerical results shown above also demonstrate that the optimal rib width for a given pitch width is only sensitive to the rib-electrode contact resistance. That allows us to obtain simple expressions for the optimal rib widths, providing an easy to use guidance for the broad SOFC engineering community.

The optimal rib width for a given contact resistance and a given pitch width may be obtained by changing the rib width to achieve the maximum cell current density. The optimal rib widths for practical contact resistances and pitch widths are shown in Fig. 7. As may be seen from Fig. 7a, the optimal anode rib width for a given pitch width is dependent on the contact resistance approximately linearly. Moreover, the slope in the linear relationship is roughly independent of the pitch width. Similarly, the optimal anode rib width for a given contact resistance is also found to be dependent approximately linearly on the pitch width with the slope independent of the contact resistance. Consequently, the optimal anode rib width may be expressed as:

$$d_{rib} = A + B \times d_{pitch} + C \times ASR_{contact} \quad (30)$$

The three parameters in Eq. (30) for the optimal anode rib width may be obtained by fitting as $A^{an} = 0.21$ mm, $B^{an} = 0.42$, $C^{an} = 10$ mm Ω^{-1} cm^{-2}. As will be discussed below, Eq. (30) is also suitable for estimating the optimal cathode rib width, but the three parameters should be revised as $A^{ca} = 0.13$ mm, $B^{ca} = 0.14$, and $C^{ca} = 5.5$ mm Ω^{-1} cm^{-2}.

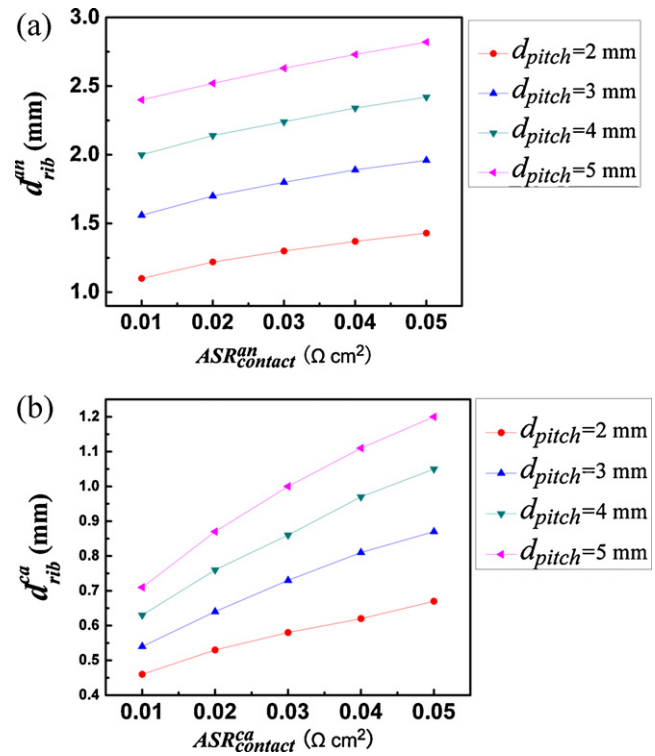

Fig. 7. Dependence of the optimal anode (cathode) rib width, d_{riban} (d_{ribca}), on the contact resistance and pitch width: (a) anode, (b) cathode.

As described above, Eq. (30) is only an approximation for the true numerical results. The usefulness of Eq. (30) for guiding the optimal anode rib width design may be vilified by the accuracy parameter, γ, defined as,

$$\gamma = \frac{i_{max} - i_{rib}}{i_{max}} \times 100\% \quad (31)$$

where i_{max} is the output current density corresponding to the numerically optimized rib width, while i_{rib} is the current density for the rib width determined analytically by Eq. (30). Fig. 8a shows the results of γ for different anode pitch widths and contact resistances. Clearly, γ is always negligibly small. Therefore, the anode rib width determined by Eq. (30) is highly optimal for engineering applications.

As shown in Fig. 7b, the optimal cathode rib width for a given pitch width is dependent on the contact resistance approximately linearly, but the slope increases with the pitch width. Similarly, the optimal cathode rib width for a given contact resistance is also found to be dependent approximately linearly on the pitch width and the slope increases with the contact resistance. It may be inferred then that Eq. (30) may not accurately represent the optimal cathode rib width. With the rib and pitch widths in mm and ASR in Ωcm^2, the cathode rib width is best fitted as,

$$d_{rib}^{ca} = 0.28 + 0.07 \times d_{pitch}^{ca} + (0.8 + 2.35 \times d_{pitch}^{ca}) \times ASR_{contact}^{ca} \quad (32)$$

However, considering the extremal property of the cell output around the optimal rib width, the deviation of the cell output from its optimal value is only quadratic on the small error of estimating the optimal rib width. It is likely then that the estimation of the optimal rib width by the simple expression of Eq. (30) with proper parameters suffices for any practical purpose. To this end, the fittings yield $A^{ca} = 0.13$ mm, $B^{ca} = 0.14$ and $C^{ca} = 5.5$ mm Ω^{-1} cm^{-2}. Fig. 8b shows the deviation of the current output with the optimal cathode rib width estimated by Eq. (30) from that with truly optimized rib width for various pitch widths and contact resistances.

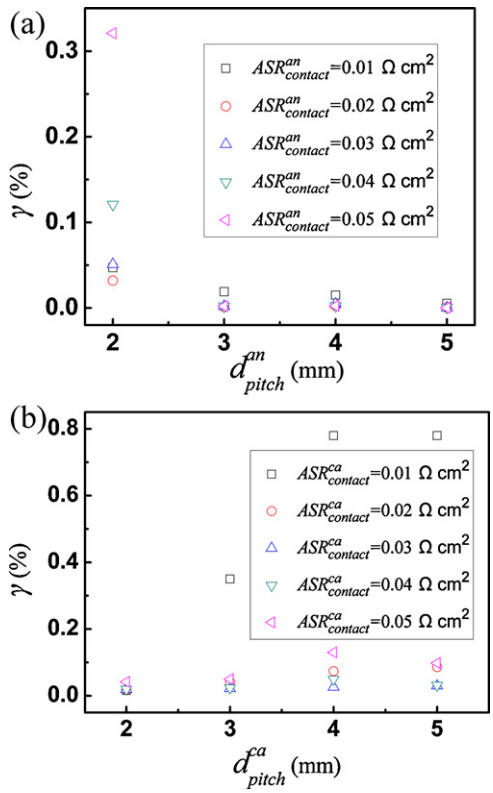

Fig. 8. Deviations of the current outputs with analytically determined rib widths from that with numerically optimized rib widths for different pitch widths and contact resistances: (a) anode, (b) cathode.

As shown in Fig. 8b, the maximal error by using Eq. (30) is less than 1% for all cases examined. The result demonstrates that the optimal cathode rib width may also be accurately estimated by Eq. (30).

4. Summary

We have described a comprehensive two dimensional mathematical model for the performance of the planar SOFC stack. The model takes into account the contact resistances between the electrodes and the interconnect ribs and the dependence of the effective electrode properties on the microstructure parameters of the porous electrodes. The impacts of the electrode rib widths are systematically examined by varying the contact resistance, fuel composition, electrode porosity, thickness and conductivity. The numerical results show conclusively that the output current density depends strongly on the rib widths and the optimal rib widths for the anode and the cathode are quite different. Nevertheless, the optimal widths for both the anode and cathode ribs are found to be only sensitive to the contact resistance and the pitch width and may be determined by the same simple analytical expression, $d_{rib} = A + B \times d_{pitch} + C \times ASR_{contact}$. For the anode, $A = 0.21$ mm, $B = 0.42$, $C = 10$ mm Ω^{-1} cm^{-2} and d_{rib} is the optimal anode rib width corresponding to a given anode pitch width, d_{pitch}, and a contact resistance at the interconnect rib and anode interface, $ASR_{contact}$. For the cathode, $A = 0.13$ mm, $B = 0.14$, $C = 5.5$ mm Ω^{-1} cm^{-2} and d_{rib} is the optimal cathode rib width corresponding to a given cathode pitch width, d_{pitch}, and a contact resistance at the interconnect rib and cathode interface, $ASR_{contact}$. The simple formula provides an easy to use guidance for the broad SOFC engineering community in designing the optimal rib-channel layout.

Acknowledgements

The financial support of the State Key Development Program for Basic Research of China (Grant No. 2012CB215405) and the National Natural Science Foundation of China (10574114) are gratefully acknowledged.

References

[1] J.W. Kim, A.V. Virkar, K.Z. Fung, K. Mehta, S.C. Singhal, Journal of the Electrochemical Society 146 (1999) 69–78.
[2] F. Zhao, A.V. Virkar, Journal of Power Sources 141 (2005) 79–95.
[3] S. de Souza, S.J. Visco, L.C. De Jonghe, Journal of the Electrochemical Society 144 (1997) L35–L37.
[4] T. Tsai, S.A. Barnett, Solid State Ionics 98 (1997) 191–196.
[5] S.D. Kim, H. Moon, S.H. Hyun, J. Moon, J. Kim, H.W. Lee, Journal of Power Sources 163 (2006) 392–397.
[6] S.D. Kim, J.J. Lee, H. Moon, S.H. Hyun, J. Moon, J. Kim, H.W. Lee, Journal of Power Sources 169 (2007) 265–270.
[7] L. Blum, W.A. Meulenberg, H. Nabielek, R. Steinberger-Wilckens, International Journal of Applied Ceramic Technology 2 (2005) 482–492.
[8] M. Kornely, A. Leonide, A. Weber, E. Ivers-Tiffée, Journal of Power Sources 196 (2011) 7209–7216.
[9] S. Jiang, J. Love, L. Apateanu, Solid State Ionics 160 (2003) 15–26.
[10] Z. Yang, G. Xia, S.P. Simner, J.W. Stevenson, Journal of the Electrochemical Society 152 (2005) A1896–A1901.
[11] S. Ahmed, C. McPheeters, R. Kumar, Journal of the Electrochemical Society 138 (1991) 2712–2718.
[12] J. Ferguson, J. Fiard, R. Herbin, Journal of Power Sources 58 (1996) 109–122.
[13] C.W. Tanner, A.V. Virkar, Journal of Power Sources 113 (2003) 44–56.
[14] Z. Lin, J. Stevenson, M. Khaleel, Journal of Power Sources 117 (2003) 92–97.
[15] Y. Ji, K. Yuan, J. Chung, Y.C. Chen, Journal of Power Sources 161 (2006) 380–391.
[16] D.H. Jeon, J.H. Nam, C.J. Kim, Journal of the Electrochemical Society 153 (2006) A406–A417.
[17] S. Liu, C. Song, Z. Lin, Journal of Power Sources 183 (2008) 214–225.
[18] S. Liu, W. Kong, Z. Lin, Energies 2 (2009) 427–444.
[19] S. Liu, W. Kong, Z. Lin, Journal of Power Sources 194 (2009) 854–863.
[20] R. Suwanwarangkul, E. Croiset, M. Fowler, P. Douglas, E. Entchev, M. Douglas, Journal of Power Sources 122 (2003) 9–18.
[21] E.A. Mason, A.P. Malinauskas, Transport in Porous Media: The Dusty Gas Model, Elsevier, New York, 1983.
[22] K. Tseronis, I. Kookos, C. Theodoropoulos, Chemical Engineering Science 63 (2008) 5626–5638.
[23] D. Chen, W. Bi, W. Kong, Z. Lin, Journal of Power Sources 195 (2010) 6598–6610.
[24] A. Ali, X. Wen, K. Nandakumar, J. Luo, K.T. Chuang, Journal of Power Sources 185 (2008) 961–966.
[25] V.M. Janardhanan, V. Heuveline, O. Deutschmann, Journal of Power Sources 178 (2008) 368–372.
[26] D. Chen, Z. Lin, H. Zhu, R.J. Kee, Journal of Power Sources 191 (2009) 240–252.
[27] X. Chen, S. Chan, K. Khor, Electrochimica Acta 49 (2004) 1851–1861.
[28] J. Wu, D. McLachlan, Physical Review B 56 (1997) 1236–1248.
[29] P. Costamagna, P. Costa, V. Antonucci, Electrochimica Acta 43 (1998) 375–394.
[30] M. Suzuki, T. Oshima, Powder Technology 44 (1985) 213–218.
[31] D. Bouvard, F. Lange, Acta Metallurgica et Materialia 39 (1991) 3083–3090.
[32] Y. Shi, N. Cai, C. Li, Journal of Power Sources 164 (2007) 639–648.
[33] P. Costamagna, K. Honegger, Journal of the Electrochemical Society 145 (1998) 3995–4007.
[34] H. Zhu, R.J. Kee, Journal of the Electrochemical Society 155 (2008) B715–B729.
[35] W. Wei, W. Chen, D.G. Ivey, Journal of Power Sources 186 (2009) 428–434.
[36] Y. Guan, Y. Gong, W. Li, J. Gelb, L. Zhang, G. Liu, X. Zhang, X. Song, C. Xia, Y. Xiong, Journal of Power Sources 196 (2011) 10601–10605.